

Multidimensional Dissipation for Upwind Schemes: Stability and Applications to Gas Dynamics

Richard Sanders^{*,1}, Eric Morano,^{†,2} and Marie-Claude Druguet^{‡,3}

^{*}*Department of Mathematics, University of Houston, Houston, Texas 77204-3476; †Graduate Aeronautical Laboratories, MS 205-45, California Institute of Technology, Pasadena, California 91125; and ‡Département Milieux Hors d'Équilibre, IUSTI, UMR-CNRS 6595, Université de Provence, Technopôle de Château-Gombert, 13453 Marseille Cedex 13, France*

Received April 8, 1997; revised June 4, 1998

In this work, we identify an instability in strictly upwind finite difference schemes when they are applied to the Euler equations in more than one space dimension. We suggest that the well known *carbuncle phenomenon* is a manifestation of this instability. The usual dimension by dimension extension of one-dimensional upwind schemes to the multidimensional equations of gas dynamics often yields poorly resolved stationary (or slowly moving) shocks when applied to high Mach number grid aligned flows on structured grids. Through linear analysis, we show that this failure is an instability which is the result of inadequate crossflow dissipation offered by strictly upwind schemes. In addition, we offer a new parameter free and easy to implement multidimensional, upwind dissipation modification that provides sufficient crossflow dissipation to eliminate the instability. This new approach is applied to the problem of simulating a three-dimensional, axisymmetric, hypersonic, chemically reacting air flow typically encountered during spacecraft reentry. © 1998 Academic Press

1. INTRODUCTION

In this paper we focus on the problem of solving the multidimensional Euler equations on structured grids by finite volume schemes based on *strictly* upwind numerical flux functions. Examples of these upwind fluxes include Godunov's flux [5] and Roe's flux [17]. When applied to the one-dimensional Euler equations, these schemes have the desirable property of accurately resolving shock waves as well as contact discontinuities. Expansion

¹ Supported in part by NASA Grant NAG 9-896 and Texas ARP Grant 003652-229.

² Supported in part by Texas ARP Grant 003652-229 and the U. of Houston ISSO postdoctoral fellowship.

³ Supported by the ESA postdoctoral fellowship while in residence at the University of Houston.

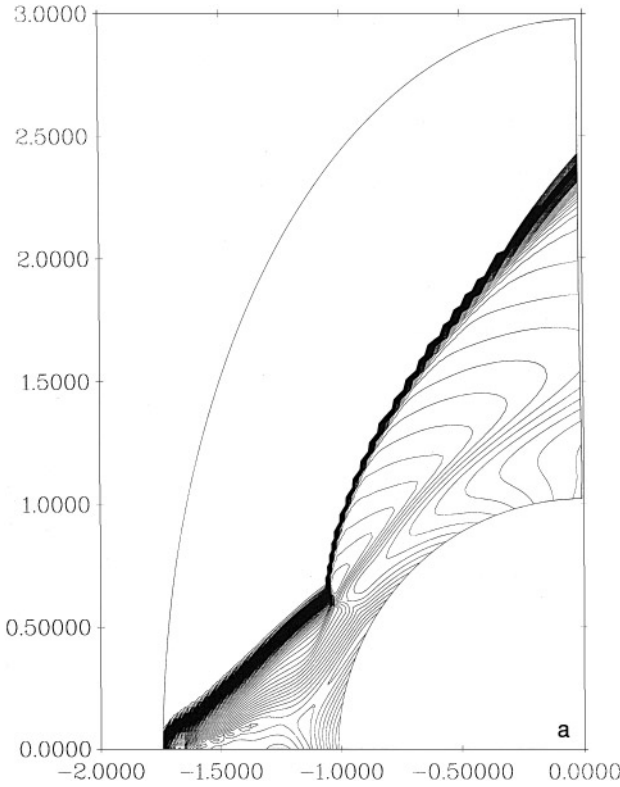
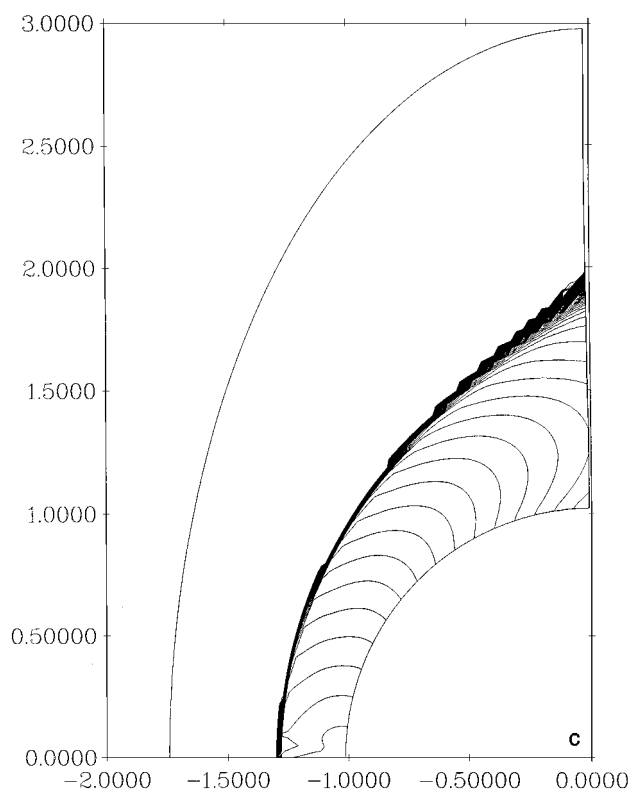
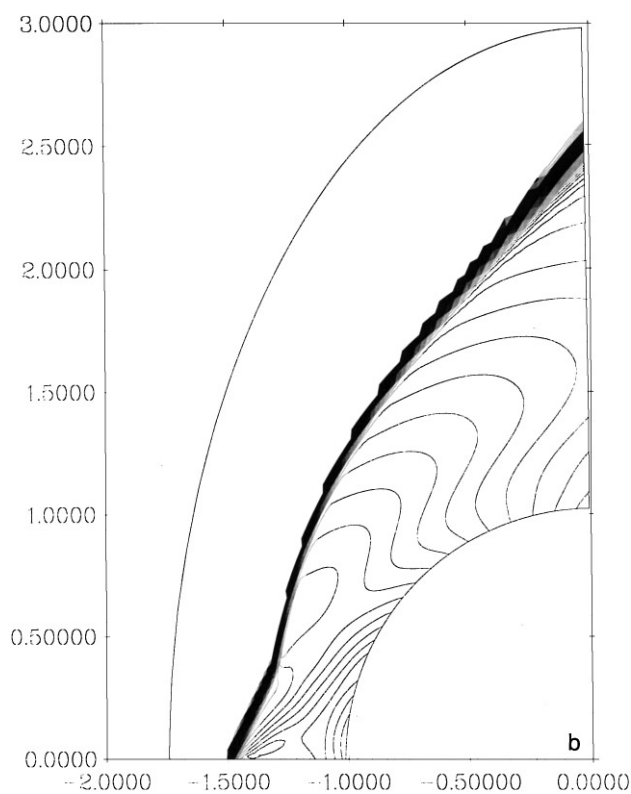


FIG. 1. Mach number isocontours for the 2D Mach 15.3 cylinder: (a) First-order Roe's scheme with no entropy correction; (b) First-order Roe's scheme with a typical 1D entropy correction; (c) First-order Godunov's scheme.

waves can generally be well resolved either by use of entropic schemes such as Godunov's or Osher's [11], or by some suitable modification to nonentropic schemes such as Roe's. However, naively inserting a one-dimensional, strictly upwind numerical flux function into a multidimensional finite volume formulation may often lead to a seriously flawed numerical algorithm. It is often observed that strong slowly moving or stationary shocks aligned with the spatial grid break down in a totally nonphysical manner. The *carbuncle phenomenon* [2,13,21] is the name often used to refer to a stationary bow shock that contains a spurious bump. The work of Quirk [15] is particularly enlightening here. In Fig. 1, we illustrate this flaw by the well-known example of a high speed, here Mach 15.3, inviscid flow around a two-dimensional cylinder. In Fig. 1a is the result from a first-order Roe scheme without entropy correction. In Fig. 1b is the result of the Roe's scheme this time employing a standard one-dimensional entropy correction (see Eq. (9b) in Section 2). Finally, in Fig. 1c is the result from the first-order Godunov scheme before convergence to steady state. While the carbuncle is less noticeable in the Godunov result, at this time there is still a noticeable *glitch* at the leading edge of the bow shock. Eventually, this glitch will weaken and propagate downstream along the shock.

The usual procedure to cure the carbuncle flaw is based on some *ad hoc*, parameter-based switch to an extremely dissipative convective flux such as Lax–Friedrichs (or some other nonstrictly upwind flux) in regions deemed as susceptible to the carbuncle phenomenon. Beside introducing a great deal of complexity to the computer program, this approach

**FIG. 1—Continued**

generally leads to a scheme that has excessive numerical dissipation in regions where it is particularly harmful, such as boundary layers—shock interaction, slip surfaces, and regions of multicomponent nonequilibrium.

The contents of this paper are organized as follows. Some preliminary setup is contained in Section 2. Additionally, numerical dissipation is discussed, the term strictly upwind is defined, and several well-known two-point numerical fluxes are classified. In Sections 3 and 4, we explore what we believe is compelling evidence as to the cause of the carbuncle phenomenon. Section 3 is devoted to numerical evidence and Section 4 is devoted to analytical evidence. We show that the truncation error equation to upwind schemes applied to the Euler equations is linearly unstable when applied to certain flows with strongly *grid-aligned* stationary shocks. We use the term grid-aligned shocks to denote planar shocks that are perpendicular to the flow direction (e.g., a 1D shock embedded in 2D). It is our belief that the bow shock problem illustrated above is in reality a grid-aligned shock problem. The main topic of Section 5 is the introduction and analysis of a multidimensional dissipation which is shown to eliminate the carbuncle flaw in all presented examples. As will be seen, this dissipation is supported almost entirely within shock layers and at the same time leaves perfectly grid aligned shocks resolved exactly the same as would come from the one-dimensional calculation. In Section 6, the method of Section 5 is extended to high order schemes and is applied to a high speed flow with nonequilibrium multicomponent chemistry.

2. STRICTLY UPWIND DISSIPATION AND THE EULER EQUATIONS

Finite volume schemes for solving divergence form hyperbolic systems in more than one space dimension are obtained by considering the control volume balance equation

$$\frac{\partial}{\partial t} \int_C \mathbf{U} dx + \int_{\partial C} \mathbf{F}(\mathbf{U}) \cdot \mathbf{n} d\sigma = 0, \quad (1)$$

where C denotes a control volume and \mathbf{n} its outward normal vector. Throughout this work, we assume that the space partitioning is logically rectangular. The usual approach taken to construct a *first-order* finite volume scheme from this formulation is to regard \mathbf{U} as cellwise constant and then replace the cell boundary fluxes $\mathbf{F}(\mathbf{U}) \cdot \mathbf{n}$ by a one-dimensional, two-point, numerical flux function $h_{\mathbf{F} \cdot \mathbf{n}}(\mathbf{U}_L, \mathbf{U}_R)$, where \mathbf{U}_L denotes the value of the solution within cell C and \mathbf{U}_R the value of the solution in the outward adjacent cell. Consistency is enforced by requiring $h_{\mathbf{F} \cdot \mathbf{n}}(\mathbf{U}, \mathbf{U}) = \mathbf{F}(\mathbf{U}) \cdot \mathbf{n}$. In this context, any one-dimensional, Lipschitz continuous, two-point numerical flux function takes the general form

$$h_{\mathbf{F} \cdot \mathbf{n}}(\mathbf{U}_L, \mathbf{U}_R) = \frac{1}{2} [\mathbf{F} \cdot \mathbf{n}(\mathbf{U}_L) + \mathbf{F} \cdot \mathbf{n}(\mathbf{U}_R) - M(\mathbf{U}_L, \mathbf{U}_R, \mathbf{n})(\mathbf{U}_R - \mathbf{U}_L)]. \quad (2)$$

The generality of the specific form indicated in (2) is seen by defining the vector dissipation $D(\mathbf{U}_L, \mathbf{U}_R, \mathbf{n})$ via the relation

$$h_{\mathbf{F} \cdot \mathbf{n}}(\mathbf{U}_L, \mathbf{U}_R) = \frac{1}{2} [\mathbf{F} \cdot \mathbf{n}(\mathbf{U}_L) + \mathbf{F} \cdot \mathbf{n}(\mathbf{U}_R)] - D(\mathbf{U}_L, \mathbf{U}_R, \mathbf{n})$$

and by noting that, since flux consistency implies $D(\mathbf{U}, \mathbf{U}, \mathbf{n}) = 0$, the fundamental theorem of calculus implies

$$D(\mathbf{U}_L, \mathbf{U}_R, \mathbf{n}) = \int_0^1 \frac{d}{d\theta} D(\mathbf{U}_M - \Delta \mathbf{U}_M \theta, \mathbf{U}_M + \Delta \mathbf{U}_M \theta) d\theta,$$

where $\mathbf{U}_M = \frac{1}{2}(\mathbf{U}_R + \mathbf{U}_L)$ and $\Delta\mathbf{U}_M = \frac{1}{2}(\mathbf{U}_R - \mathbf{U}_L)$. (For nondifferentiable but Lipschitz numerical fluxes, this is interpreted in an a.e. sense.) From this, the chain rule yields a formula for the dissipation matrix $M(\mathbf{U}_L, \mathbf{U}_R, \mathbf{n})$.

We use the expression *strictly upwind* to signify two-point, numerical flux functions whose dissipation matrices satisfy

$$M(\mathbf{U}, \mathbf{U}, \mathbf{n}) = |(\mathbf{F} \cdot \mathbf{n})'(\mathbf{U})| \equiv R(\mathbf{U}, \mathbf{n})\Lambda(\mathbf{U}, \mathbf{n})R^{-1}(\mathbf{U}, \mathbf{n}), \quad (3)$$

where $\Lambda(\mathbf{U}, \mathbf{n})$ and $R(\mathbf{U}, \mathbf{n})$ are the matrices of eigenvalues, respectively right eigenvectors, to the Jacobian of $\mathbf{F}(\mathbf{U}) \cdot \mathbf{n}$. With this definition, we find that the *truncation error equation* for all continuous in time finite volume schemes employing strictly upwind numerical flux functions take the form

$$\frac{\partial \mathbf{U}}{\partial t} + \frac{\partial}{\partial x}(f(\mathbf{U})) + \frac{\partial}{\partial y}(g(\mathbf{U})) = \frac{1}{2}\Delta x \frac{\partial}{\partial x} \left(|A(\mathbf{U})| \frac{\partial \mathbf{U}}{\partial x} \right) + \frac{1}{2}\Delta y \frac{\partial}{\partial y} \left(|B(\mathbf{U})| \frac{\partial \mathbf{U}}{\partial y} \right), \quad (4)$$

on a uniform two-dimensional cartesian grid. Above, $\mathbf{F}(\mathbf{U}) = (f(\mathbf{U}), g(\mathbf{U}))$, and the strictly upwind dissipation matrices are given by $|A(\mathbf{U})| = |f'(\mathbf{U})|$ and $|B(\mathbf{U})| = |g'(\mathbf{U})|$. Δx and Δy represent a measure of grid refinement. It is important to stress that all schemes employing two-point strictly upwind numerical flux functions share this same truncation error equation. It should also be noted that for these schemes, the dissipation matrices $|A(\mathbf{U})|$ or $|B(\mathbf{U})|$ fail to be of full rank when one or more eigenvalues to $f'(\mathbf{U})$ or $g'(\mathbf{U})$ vanish.

The two-dimensional, multicomponent, Euler equations for a compressible chemically reacting gas are given by

$$\frac{\partial \mathbf{U}}{\partial t} + \nabla \cdot \mathbf{F}(\mathbf{U}) = \frac{\partial}{\partial t} \begin{pmatrix} \rho_1 \\ \vdots \\ \rho_n \\ \rho u \\ \rho v \\ \rho e \end{pmatrix} + \frac{\partial}{\partial x} \begin{pmatrix} \rho_1 u \\ \vdots \\ \rho_n u \\ \rho u^2 + P \\ \rho uv \\ (\rho e + P)u \end{pmatrix} + \frac{\partial}{\partial y} \begin{pmatrix} \rho_1 v \\ \vdots \\ \rho_n v \\ \rho uv \\ \rho v^2 + P \\ (\rho e + P)v \end{pmatrix} = \Omega, \quad (5)$$

where ρ_s is the partial density of the fluid's s th chemical species, $\rho = \sum \rho_s$ is the fluid's total density, $\mathbf{V} = (u, v)$ is its velocity, and e is the total energy per unit mass. The scalar pressure P is given as a function of the state variables ρ_s and the internal energy per unit mass $\epsilon = e - \frac{1}{2}|\mathbf{V}|^2$. The chemical reaction rate Ω is also a function of ρ_s and ϵ . The flux Jacobians of the Euler equations have real eigenvalues and are diagonalizable under reasonable equations of state. The eigenvalues of $\mathbf{F}'_x(\mathbf{U})$ (the x direction flux Jacobian) are $u \pm c$ and u , where the latter eigenvalue has multiplicity $n + 1$ and the speed of sound c is given by

$$c^2 = \frac{1}{\rho} \sum_s \rho_s P_{\rho_s} + \frac{1}{\rho^2} P P_\epsilon > 0 \quad \text{for physical equations of state.} \quad (6m)$$

The fields associated to eigenvalues $\lambda_\pm = u \pm c$ are *genuinely nonlinear*,

$$\nabla_{\mathbf{U}} \lambda_\pm \cdot \mathbf{r}_\pm \neq 0,$$

whereas the $n + 1$ fields associated to eigenvalue $\lambda = u$ are *linearly degenerate*

$$\nabla_{\mathbf{U}} \lambda \cdot \mathbf{r} \equiv 0;$$

see [8]. In the last section, the full multicomponent Euler equations are studied. Until then, only a single component ($n = 1$), diatomic, perfect gas is considered, in which case $P = (\gamma - 1)\rho\epsilon$, where $\gamma = 1.4$ is the ratio of specific heats, and

$$c^2 = \gamma(\gamma - 1)\epsilon. \quad (6s)$$

We conclude this section by checking several well-known two-point numerical flux functions to determine which are and which are not strictly upwind when applied to the two-dimensional, single component Euler equations. The rotational invariance of the Euler equations in several space dimensions allows us to restrict our attention to the x -directional flux only. This is denoted by $f(\mathbf{U})$ below. It is a straightforward exercise to confirm that a two-point numerical flux $h_f(\mathbf{U}_L, \mathbf{U}_R)$ consistent to $f(\mathbf{U})$ is strictly upwind if and only if for all admissible states \mathbf{U}_L and \mathbf{U}_R sufficiently close together

$$(f(\mathbf{U}_L) + f(\mathbf{U}_R)) - 2h_f(\mathbf{U}_L, \mathbf{U}_R) = |f'(\bar{\mathbf{U}})|(\mathbf{U}_R - \mathbf{U}_L) + O(|\mathbf{U}_R - \mathbf{U}_L|^2), \quad (7)$$

where $\bar{\mathbf{U}} = \frac{1}{2}(\mathbf{U}_L + \mathbf{U}_R)$. That is, if (7) is satisfied for a particular numerical flux $h_f(\mathbf{U}_L, \mathbf{U}_R)$, then h_f is strictly upwind. Otherwise, h_f is not strictly upwind.

The first numerical flux we investigate is the van Leer upwind flux [20]. It is given by

$$h_f(\mathbf{U}_L, \mathbf{U}_R) = f^+(\mathbf{U}_L) + f^-(\mathbf{U}_R), \quad (8.vL)$$

where

$$f^+(\mathbf{U}) = \begin{cases} f(\mathbf{U}), & \text{if } u \geq c, \\ 0, & \text{if } u \leq -c, \\ \begin{pmatrix} \frac{1}{4}\rho c(u/c + 1)^2 \equiv f_1^+ \\ f_1^+((\gamma - 1)u + 2c)/\gamma \\ f_1^+v \\ f_1^+ \left(\frac{((\gamma - 1)u + 2c)^2}{2(\gamma^2 - 1)} + \frac{v^2}{2} \right) \end{pmatrix}, & \text{otherwise,} \end{cases}$$

and

$$f^-(\mathbf{U}) = f(\mathbf{U}) - f^+(\mathbf{U}).$$

If states \mathbf{U}_L and \mathbf{U}_R are both supersonic, then clearly the strictly upwind condition (7) above is satisfied. However, for subsonic flows, the van Leer flux fails to be strictly upwind. This can easily be seen by considering particular states \mathbf{U}_L and \mathbf{U}_R of the form

$$\mathbf{U}_{L,R} = \begin{pmatrix} \bar{\rho} \\ 0 \\ 0 \\ \bar{\rho}\bar{e} \end{pmatrix} \pm \begin{pmatrix} 0 \\ 0 \\ \delta\bar{\rho} \\ 0 \end{pmatrix},$$

which defines a weak stationary shear wave. By observing that the second vector above is an eigenvector to $f'(\bar{\rho}, 0, 0, \bar{\rho}\bar{e})$ associated to eigenvalue $u = 0$, one finds that the right-hand side of (7) reduces to $O(|\mathbf{U}_R - \mathbf{U}_L|^2)$. A simple calculation shows the left-hand side reduces to $c/2(\mathbf{U}_R - \mathbf{U}_L)$. Thus, the van Leer flux fails to satisfy the strictly upwind criterion for all admissible states.

The second numerical flux we investigate is the Godunov upwind flux [5]. It is given by

$$h_f(\mathbf{U}_L, \mathbf{U}_R) = f(\mathfrak{R}(\mathbf{U}_L, \mathbf{U}_R)), \quad (8.G)$$

where $\mathfrak{R}(\mathbf{U}_L, \mathbf{U}_R)$ denotes the solution to the Riemann problem defined by left and right states $\mathbf{U}_L, \mathbf{U}_R$ along the vertical space-time ray $x/t = 0$. The Riemann problem here is resolved into four waves (actually three discernible waves) and five constant states $\mathbf{U}_L = \mathbf{U}_0, \mathbf{U}_1, \dots, \mathbf{U}_4 = \mathbf{U}_R$. It is shown in [8] for \mathbf{U}_L and \mathbf{U}_R sufficiently close together that

$$\mathbf{U}_k = \mathbf{U}_{k-1} + \mathbf{l}_k(\bar{\mathbf{U}}) \cdot (\mathbf{U}_R - \mathbf{U}_L) \mathbf{r}_k(\bar{\mathbf{U}}) + O(|\mathbf{U}_R - \mathbf{U}_L|^2),$$

where the left eigenvectors \mathbf{l}_k are normalized so that $\mathbf{l}_k \cdot \mathbf{r}_k = 1$. Moreover, by using the weak formulation of the Riemann problem, one can show that

$$f(\mathfrak{R}(\mathbf{U}_L, \mathbf{U}_R)) = \frac{1}{2} \left(f(\mathbf{U}_L) + f(\mathbf{U}_R) - \sum_{k=1}^4 W(\mathbf{U}_{k-1}, \mathbf{U}_k) \right),$$

where

$$W(\mathbf{U}_{k-1}, \mathbf{U}_k) = \begin{cases} |s(\mathbf{U}_{k-1}, \mathbf{U}_k)|(\mathbf{U}_k - \mathbf{U}_{k-1}), & \text{if wave } k \text{ is a shock,} \\ \int_{\lambda_k(\mathbf{U}_{k-1})}^{\lambda_k(\mathbf{U}_k)} |\xi| \mathbf{r}_k(\xi) d\xi, & \text{if wave } k \text{ is a rarefaction,} \\ |\lambda_k(\mathbf{U}_k)|(\mathbf{U}_k - \mathbf{U}_{k-1}), & \text{if wave } k \text{ is linearly degenerate.} \end{cases}$$

Above, the eigenvectors for the genuinely nonlinear fields (in particular the rarefaction waves) have been normalized so that $\nabla_{\mathbf{U}} \lambda_k \cdot \mathbf{r}_k = 1$. Therefore,

$$\lambda_k(\mathbf{U}_k) = \lambda_k(\mathbf{U}_{k-1}) + \mathbf{l}_k(\bar{\mathbf{U}}) \cdot (\mathbf{U}_R - \mathbf{U}_L) + O(|\mathbf{U}_R - \mathbf{U}_L|^2),$$

which shows

$$\int_{\lambda_k(\mathbf{U}_{k-1})}^{\lambda_k(\mathbf{U}_k)} |\xi| \mathbf{r}_k(\xi) d\xi = |\lambda_k(\bar{\mathbf{U}})| \mathbf{l}_k(\bar{\mathbf{U}}) \cdot (\mathbf{U}_R - \mathbf{U}_L) \mathbf{r}_k(\bar{\mathbf{U}}) + O(|\mathbf{U}_R - \mathbf{U}_L|^2);$$

$s(\mathbf{U}_{k-1}, \mathbf{U}_k)$ above denotes the shock speed of the shock defined by states \mathbf{U}_{k-1} and \mathbf{U}_k . It is also shown in [8] for states \mathbf{U}_L and \mathbf{U}_R sufficiently close together that

$$s(\mathbf{U}_{k-1}, \mathbf{U}_k) = \lambda_k(\bar{\mathbf{U}}) + O(|\mathbf{U}_R - \mathbf{U}_L|).$$

Combining these facts together, we easily compute that

$$\sum_{k=1}^4 W(\mathbf{U}_{k-1}, \mathbf{U}_k) = |f'(\bar{\mathbf{U}})|(\mathbf{U}_R - \mathbf{U}_L) + O(|\mathbf{U}_R - \mathbf{U}_L|^2),$$

thereby confirming that the Godunov flux is strictly upwind.

A straightforward modification of the previous argument will also establish that the Osher–Solomon flux [11] is strictly upwind.

We lastly consider the numerical flux of Roe [17] and some of its entropy correction variants. The Roe numerical flux is given by

$$h_f(\mathbf{U}_L, \mathbf{U}_R) = \frac{1}{2}(f(\mathbf{U}_L) + f(\mathbf{U}_R) - |f'(\mathbf{U}_M)|(\mathbf{U}_R - \mathbf{U}_L)), \quad (8.R)$$

where \mathbf{U}_M denotes the Roe average middle state. For the two-dimensional, single-component, perfect gas equations, \mathbf{U}_M is determined by

$$\rho_M = \frac{1}{4}(\sqrt{\rho_L} + \sqrt{\rho_R})^2 \quad q_M = \frac{\sqrt{\rho_L} q_L + \sqrt{\rho_R} q_R}{\sqrt{\rho_L} + \sqrt{\rho_R}},$$

where q represents u , v , or enthalpy $H = e + P/\rho$. Clearly, this scheme is strictly upwind. Some variations are obtained as follows: Replace $|f'(\mathbf{U}_M)|$ above by

$$R(\bar{\mathbf{U}})|\tilde{\Lambda}(\mathbf{U}_L, \mathbf{U}_R)|R^{-1}(\bar{\mathbf{U}}),$$

where $\bar{\mathbf{U}}$ is either the Roe average of \mathbf{U}_L and \mathbf{U}_R , or perhaps the simple average $\bar{\mathbf{U}} = \frac{1}{2}(\mathbf{U}_L + \mathbf{U}_R)$. (The midpoint average is considerably easier to incorporate into a multi-component calculation with extremely complicated equations of state.) One-dimensional entropy corrections can be developed by taking $|\tilde{\Lambda}(\mathbf{U}_L, \mathbf{U}_R)| = \text{diag}(|\tilde{\lambda}_l|)$ with

$$|\tilde{\lambda}_l| = |\lambda_l(\bar{\mathbf{U}})| + \eta, \quad (9a)$$

$$|\tilde{\lambda}_l| = \max(|\lambda_l(\bar{\mathbf{U}})|, \eta), \quad (9b)$$

$$|\tilde{\lambda}_l| = \begin{cases} |\lambda_l(\bar{\mathbf{U}})|, & \text{if } |\lambda_l(\bar{\mathbf{U}})| \geq 2\eta, \\ |\lambda_l(\bar{\mathbf{U}})|^2/4\eta + \eta, & \text{otherwise,} \end{cases} \quad (9c)$$

where $\eta = \eta(\mathbf{U}_L, \mathbf{U}_R) \geq 0$ [6]. Clearly, if $\eta(\mathbf{U}_L, \mathbf{U}_R) = O(|\mathbf{U}_R - \mathbf{U}_L|)$, then all resulting modified schemes above are strictly upwind. For the single component or multicomponent Euler equations, a natural choice for η is

$$\begin{aligned} \eta(\mathbf{U}_L, \mathbf{U}_R) &= \frac{1}{2} \max_l (|\lambda_l(\mathbf{U}_R) - \lambda_l(\mathbf{U}_L)|) \\ &= \frac{1}{2} (|u_R - u_L| + |c_R - c_L|). \end{aligned} \quad (10)$$

All modifications to the basic Roe numerical flux given in (9)–(10) above adequately eliminate the often observed *expansion shock* problem associated to the unmodified scheme. However, none adequately resolve the carbuncle problem. Figure 1b depicts the result of modification (9b) to Roe's scheme compared to the result of the unmodified scheme depicted in Fig. 1a.

The grid used to generate the results in Fig. 1 is somewhat rough—unintentionally so originally. It was generated from a smooth coarser grid by linear bisection with boundary points exactly fitted to the cylinder. Therefore, every other interior grid point differs from a smooth grid by at most $O(\Delta x^2)$. Surprisingly, this small degree of grid error is sufficient to obliterate the true solution of the flow problem. What is even more surprising, the results depicted in Fig. 1 are not confined to the Roe scheme alone. All strictly upwind schemes discussed above yield more or less the same poor results on the given grid. Results coming from van Leer's flux and from the Lax–Friedrichs flux, on the other hand do not exhibit this flaw.

3. INSTABILITY FROM STRICTLY UPWIND SCHEMES: NUMERICAL EVIDENCE

Two-point, strictly upwind numerical flux functions were defined in the previous section, and it was seen there that all two-dimensional finite volume schemes employing these fluxes share the same truncation error equation. In particular, (4) is the truncation error equation for a continuous in time, strictly upwind, approximating scheme on a uniform rectangular grid. The following observation is informative when (4) is applied to the Euler equations. If the initial data is one-dimensional and is associated to a one-dimensional (in x) and slowly moving viscous shock profile (viscous with respect to the numerical viscosity $\frac{1}{2}\Delta x|A|$), then both numerical viscosities $\frac{1}{2}\Delta x|A|$ and $\frac{1}{2}\Delta y|B|$ simultaneously fail to be of full rank at some point along the viscous shock profile. The matrix $|B|$ has two eigenvalues $|v| = 0$ everywhere. The entropy condition requires that data at infinity associated to a k -shock ($k = 1$ or 4) profile satisfies $\lambda_k(\mathbf{U}_{-\infty}) > s > \lambda_k(\mathbf{U}_{\infty})$, where s denotes the shock speed and λ_k is one of the acoustic eigenvalues to f' . Therefore, if s is sufficiently small, $|A|$ also fails to be of full rank at some point along the shock profile since, at some point, $\lambda_k = u \pm c$ must change sign. The truncation error equation applied to the Euler equations can be shown to be linearly stable when the linearization is carried out around all admissible **constant** states. Nevertheless, this loss of numerical dissipation leads one to naturally question the stability of schemes sharing this truncation error equation when applied to perturbations of **strong** and slowly moving numerical shocks. It is precisely this situation described above that will be investigated next by a numerical example.

The first two examples of this section are set up as follows. Consider a one-dimensional shock tube with left and right states that correspond to a stationary, pressure ratio 10, 1-shock. First-order finite volume schemes employing the Roe flux, as well as the Godunov flux resolve this Riemann problem exactly on a Cartesian grid. We use this Riemann data, however, on a two-dimensional finite volume grid which is very slightly perturbed in the crossflow direction. One grid line aligned with the center of the stationary shock is modified in a mass conserving manner; see Fig. 2. Hard wall boundary conditions are enforced along the upper and lower walls:

$$(X_{i,j}, Y_{i,j}) = \begin{cases} (10 + 10^{-4} \cos(j 2\pi/20), j), & i = 10, \forall j \in [0, 40], \\ (i, j), & \text{otherwise,} \end{cases} \quad (11)$$

$$\Delta x = \Delta y = 1.$$

We then start forward Euler iteration applied to both the Roe and Godunov finite volume scheme on the perturbed grid, taking various time step sizes well within the *CFL* limit.

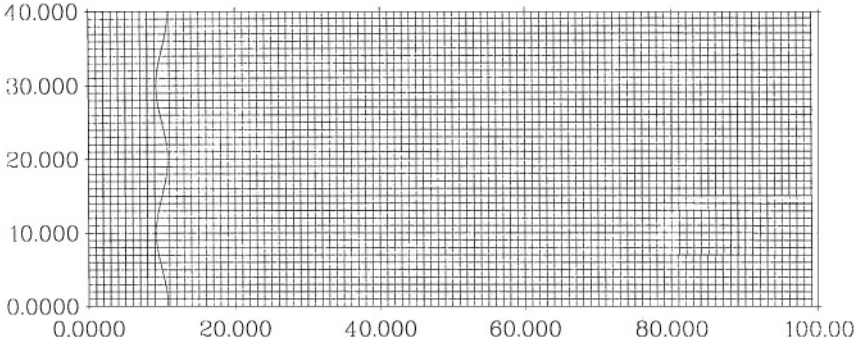


FIG. 2. The perturbed grid line is grossly exaggerated for clarity.

After several iterations the (in)famous carbuncle phenomenon appears for Godunov and Roe as depicted in Figs. 3a and 4a. Serious errors develop at the shock and propagate downstream. Figures 3b and 4b depict $\|\rho(t) - \rho(0)\|_\infty$ as a function of time. Figures 3c–e and 4c–e depict sections of $\rho(x, y, t) - \rho(x, y, 0)$ at three different times oriented tangent to and at a location immediately behind the initial shock location. These times were chosen to be at the beginning and end of the rapid growth of the density perturbation, and at a later time. Note that the grid perturbation has resulted in a seven orders of magnitude growth over a very short period of time—three more than should be expected. Various time step sizes were used, ranging from a CFL condition $\text{CFL} = 0.05$ to the largest corresponding to $\text{CFL} = 0.5$. It is interesting to note that the rate of growth of the grid perturbation, indicated in Figs. 3b and 4b, is essentially independent of time step size. For this example, we find that sections $\rho(x, y, t) - \rho(x, y, 0)$ coming from both schemes have a *characteristic* high frequency component in the crossflow (y) direction. Moreover, the nature of this is essentially independent of the frequency of the grid perturbation. Depending on the grid aspect ratio and pressure ratio of the shock conditions, we observed that it is possible to set off the instability noted above by applying grid perturbations on the order of double precision roundoff. However, we have depicted a relatively low frequency grid perturbation in these examples to help illustrate the high frequency nature of the most unstable modes. It should also be noted that for sufficiently small pressure jumps, no instability is observed. It is also interesting to note that, and probably not too surprising, the depicted results coming from both Godunov and Roe exhibit such similar pathologies when plotted as a function of time.

The next example considered here is based on Roe’s flux employing entropy modification (9c). However, instead of using (10) for the parameter η , we take η fixed and equal to 1% of the fastest wave speed present in the flow. This modification does not yield a strictly upwind flux according to our definition. Nevertheless, it is *almost* strictly upwind and is at the same time fully differentiable. The pressure ratio 10 Riemann data used in the previous two examples is no longer an exact numerical shock for this modified flux. Therefore, we determine an essentially exact numerical shock profile by one space dimensional time iteration. The resulting converged profile has an obvious middle state with a negligible downstream tail. This one-dimensional numerical shock profile is then inserted as initial data to a two-dimensional calculation employing the perturbed grid (11). After several forward Euler iterations on the perturbed grid, we again observe the rapid and unacceptable growth of certain modes; see Figs. 5a–e. The characteristic crossflow high frequency modes found in the earlier examples are again present, albeit the rate of growth of these modes is

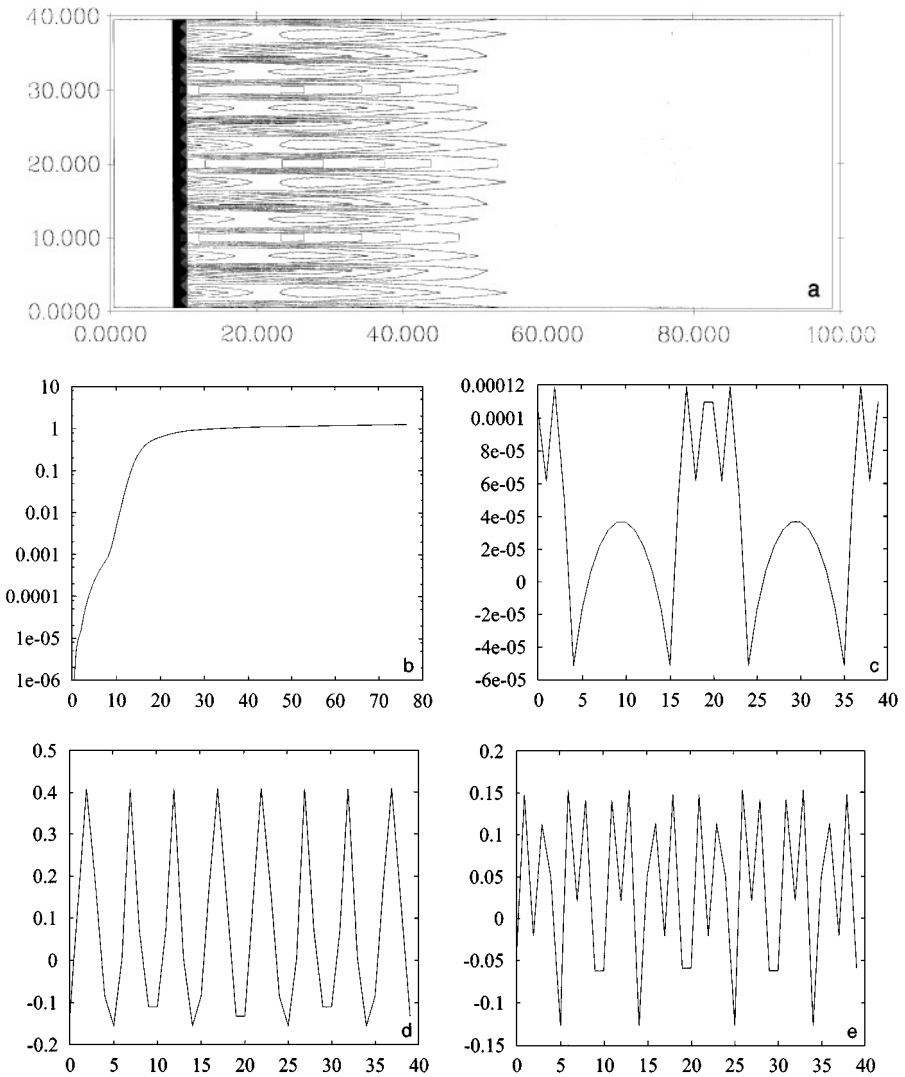


FIG. 3. 1D stationary shock breakdown from Godunov's scheme: (a) Mach contours of the deteriorated solution; (b) $\log_{10} \|\rho(t) - \rho(0)\|_\infty$ vs time; (c) $\rho(11, y, 7) - \rho(11, y, 0)$; (d) $\rho(11, y, 30) - \rho(11, y, 0)$; (e) $\rho(11, y, 76.5) - \rho(11, y, 0)$.

somewhat slower. Clearly, one should expect that varying η will have a significant effect on this example. In fact, taking η in (9c) fixed and equal to 50% of the fastest wave speed present in the flow yields the Lax–Friedrichs numerical flux. Following the same procedure for the Lax–Friedrichs flux as outlined above results in a perturbed solution that does not exhibit any large-scale deviation from the initial one-dimensional (but poorly resolved) shock profile.

The results from all strictly upwind modifications of Roe's flux defined by (9)–(10) exhibit more or less the same behavior as the example depicted in Fig. 5. The density perturbation coming from flux (9b)–(10) grows more slowly than already seen and the exponential growth is delayed by several hundred iterations. Surprisingly, the growth from schemes defined by (9a)–(10) and (9c)–(10) is faster and occurs earlier compared to (9b)–(10). Normally, one expects that a linearly unstable scheme should *blow up*

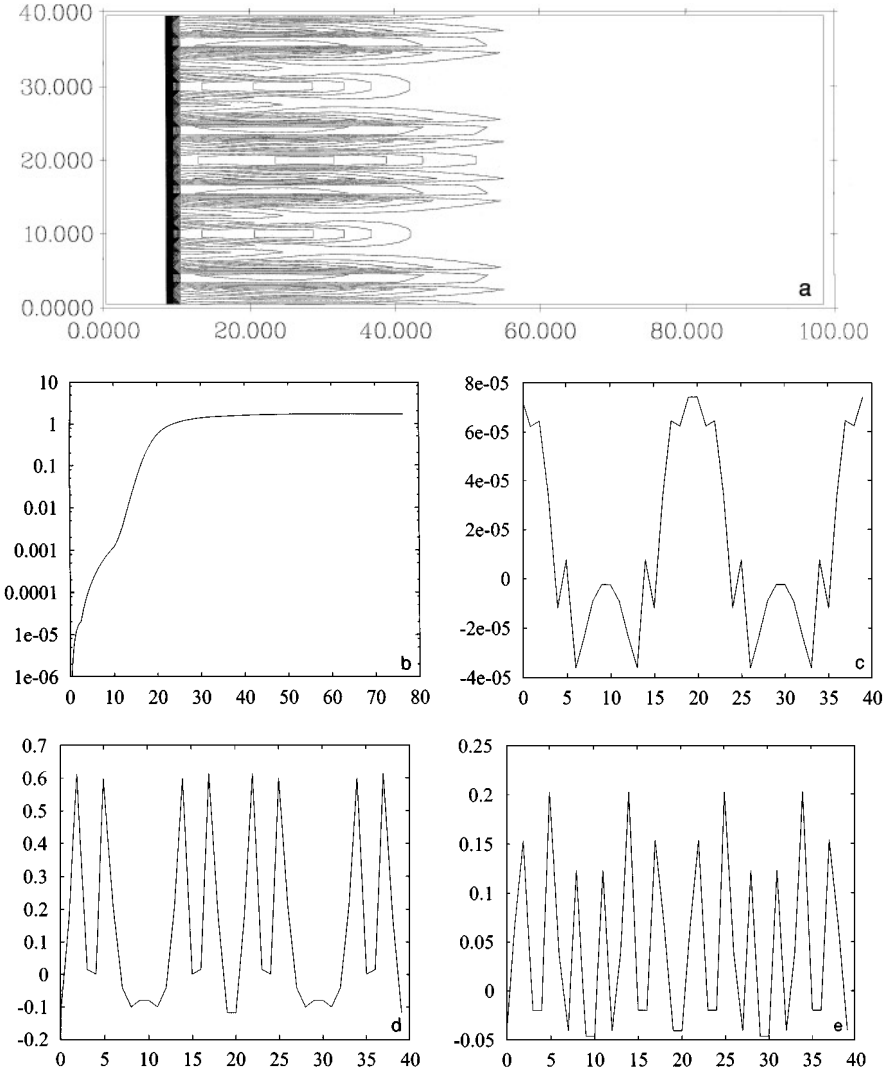


FIG. 4. 1D stationary shock breakdown from Roe's scheme: (a) Mach contours of the deteriorated solution; (b) $\log_{10} \|\rho(t) - \rho(0)\|_\infty$ vs time; (c) $\rho(11, y, 7) - \rho(11, y, 0)$; (d) $\rho(11, y, 30) - \rho(11, y, 0)$; (e) $\rho(11, y, 76.5) - \rho(11, y, 0)$.

immediately. We should remark, however, that none of the proposed modifications to Roe's scheme defined in (9)–(10) are everywhere differentiable. Moreover, the prescribed grid oscillation does not directly excite an unstable mode (see Section 4). The following test leads us to believe that the observed growth is, in fact, linear in nature. We computed $\delta = \mathbf{U}(t) - \mathbf{U}(0)$ at a time when the exponential growth first appears. The calculation was then reinitialized on the nonperturbed grid by taking initial data $\mathbf{U}(0) + \delta$ with δ scaled down so that $|\delta| \leq 10^{-5}$. This initial data yields an immediate and clearly recognizable exponential instability.

We conclude this section by considering one additional numerical flux function: van Leer's *nonstrictly* upwind flux (8.vL). Exactly the same procedure as described in the previous example is followed to set up this perturbed two-dimensional shock tube example. As was shown in the previous section, van Leer's flux offers a significant amount of shear

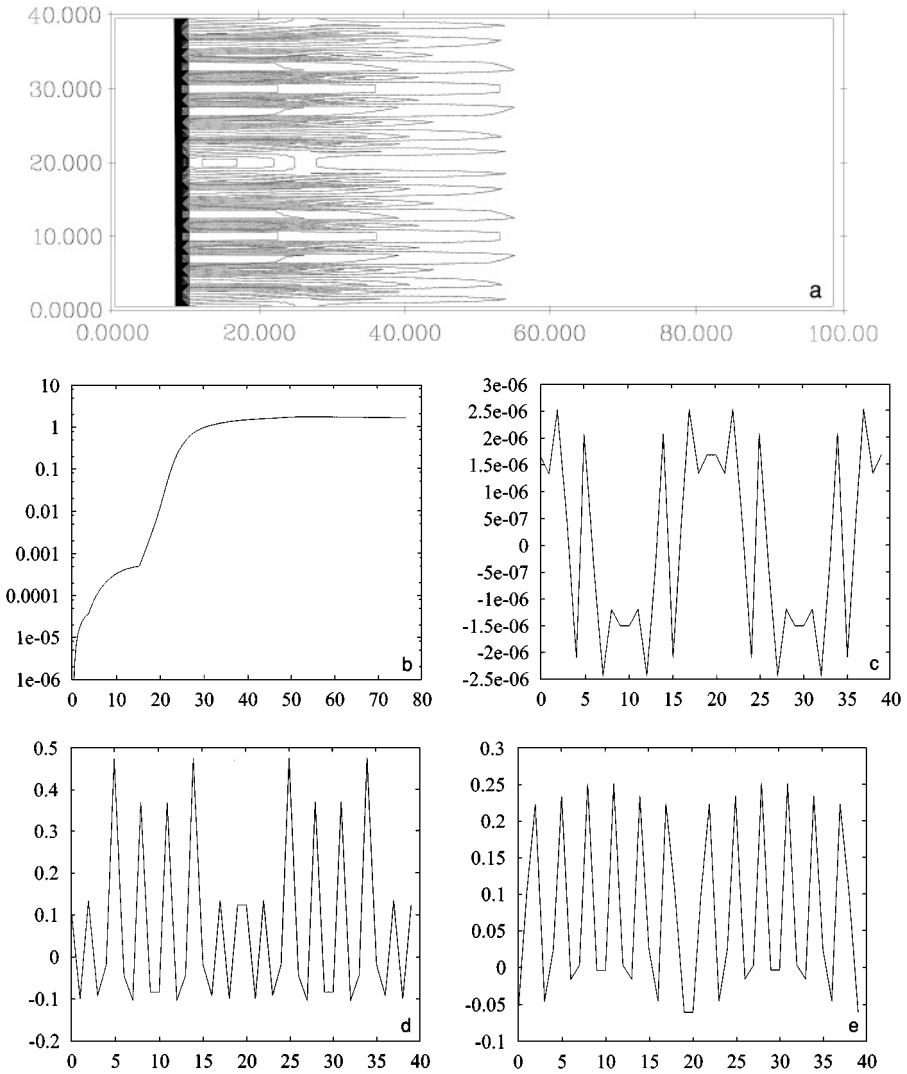


FIG. 5. 1D stationary shock breakdown from an entropy corrected variant of Roe's scheme: (a) Mach contours of the deteriorated solution; (b) $\log_{10} \|\rho(t) - \rho(0)\|_{\infty}$ vs time; (c) $\rho(11, y, 7) - \rho(11, y, 0)$; (d) $\rho(11, y, 30) - \rho(11, y, 0)$; (e) $\rho(11, y, 76.5) - \rho(11, y, 0)$.

wave dissipation. In fact, its dissipation matrix is everywhere of full rank. We should therefore expect significant smoothing of high frequency crossflow modes if any are present in the computed solution. The results for this example are depicted in Figs. 6a–e and show no evidence of the carbuncle phenomenon. (In fact, we carried this calculation out to $t = 2300$ with no further growth in the quantities already depicted.) Note that in Figs. 6c–e the crossflow sections are smooth *modulo* the grid low frequency and the density perturbations near the shock decrease in time.

4. INSTABILITY FROM STRICTLY UPWIND SCHEMES: LINEAR ANALYSIS

We analyse the instability found in the two-dimensional shock tube examples of the previous section by linear analysis. As seen there, numerical experiments indicate a strong

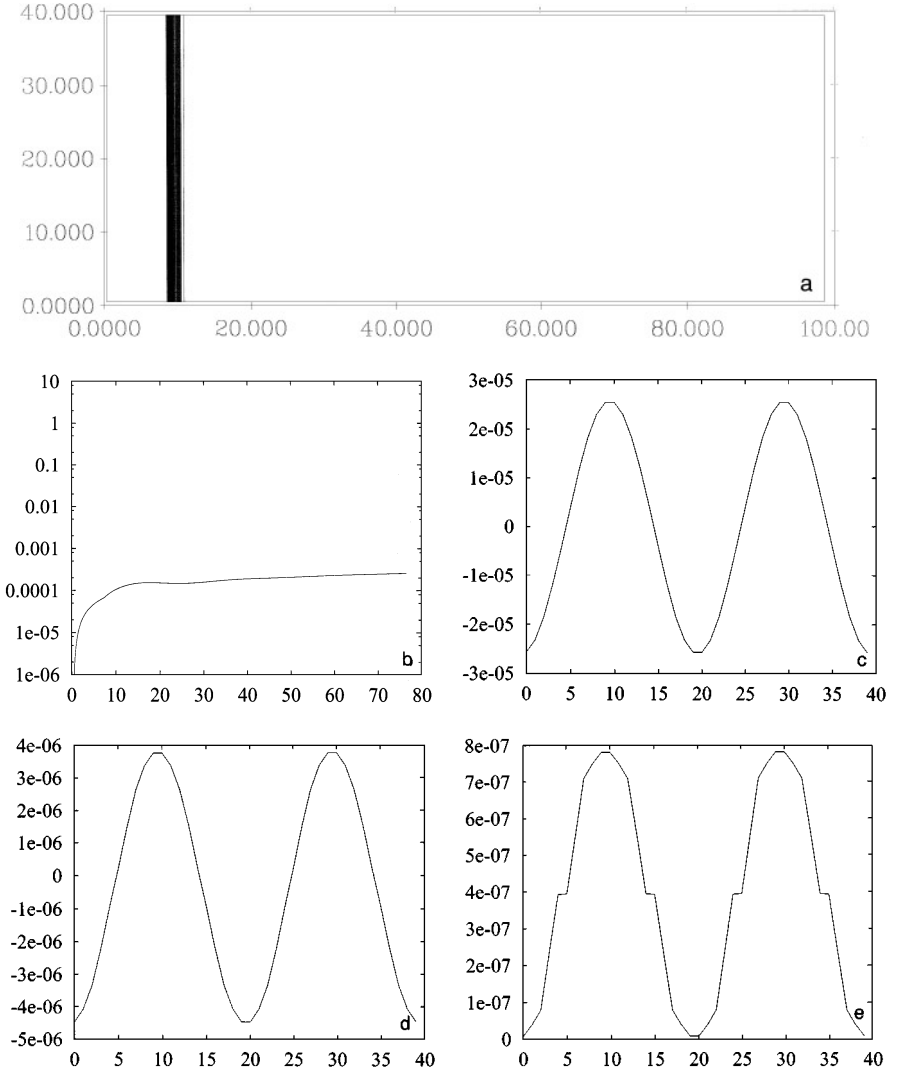


FIG. 6. Van Leer's scheme shows no evidence of breakdown: (a) Mach contours of the solution; (b) $\log_{10} \|\rho(t) - \rho(0)\|_{\infty}$ vs time; (c) $\rho(11, y, 7) - \rho(11, y, 0)$; (d) $\rho(11, y, 30) - \rho(11, y, 0)$; (e) $\rho(11, y, 76.5) - \rho(11, y, 0)$.

possibility that many, if not all, strictly upwind fluxes are somehow flawed when applied to certain flow situations and, as earlier noted, all strictly upwind schemes share a common truncation error equation (4). The goal here, therefore, is to show that the linearization of the truncation error equation is itself unstable for the given shock tube flow. We assume that (4) admits a one-dimensional stationary viscous shock profile $\mathbf{U}(x, y, t) \equiv \mathbf{T}(x)$ satisfying

$$\frac{\partial}{\partial x} f(\mathbf{T}) = \frac{1}{2} \Delta x \frac{\partial}{\partial x} \left(|A(\mathbf{T})| \frac{\partial \mathbf{T}}{\partial x} \right), \quad \lim_{x \rightarrow \pm\infty} \mathbf{T}(x) = \mathbf{U}_{\pm\infty}$$

(see [14], for example), where $[\mathbf{U}_{-\infty}, \mathbf{U}_{+\infty}]$ defines a stationary k shock. Since a stationary k -shock must satisfy $\lambda_k(\mathbf{U}_{-\infty}) > 0 > \lambda_k(\mathbf{U}_{+\infty})$, it is clear $\lambda_k(\mathbf{T})$ is zero somewhere along a trajectory joining $\mathbf{U}_{-\infty}$ to $\mathbf{U}_{+\infty}$. Therefore, at some point along $\mathbf{T}(x)$, the matrix $|f'(\mathbf{T})|$

must be singular and cannot be everywhere differentiable. For this reason, we replace the absolute value function in (3) with the smoothed version in (9c) for the associated eigenvalue λ_k , where η is taken to be constant with value $1/10$ the maximum value of $|\lambda_k|$. By doing this, the term above modelling strictly upwind dissipation $|A(\mathbf{T})| = |f'(\mathbf{T})|_s$ is nonsingular and differentiable. Linearizing about this one-dimensional solution, we find that $\mathbf{U}(x, y, t) \approx \mathbf{T}(x) + \delta(x, y, t)$, where the perturbation δ solves

$$\frac{\partial \delta}{\partial t} + \frac{\partial}{\partial x}(f'(\mathbf{T})\delta) + g'(\mathbf{T})\frac{\partial \delta}{\partial y} = \frac{1}{2}\Delta x \frac{\partial}{\partial x} \left(|A(\mathbf{T})| \frac{\partial \delta}{\partial x} + |A(\mathbf{T})'| \frac{\partial \mathbf{T}}{\partial x} \cdot \delta \right) + \frac{1}{2}\Delta y |B(\mathbf{T})| \frac{\partial^2 \delta}{\partial y^2}. \quad (12)$$

In the equation above, the matrix $|A(\mathbf{T})'| \frac{\partial \mathbf{T}}{\partial x}$ is given by

$$\left[|A(\mathbf{T})'| \frac{\partial \mathbf{T}}{\partial x} \right]_{i,j} = \sum_k \frac{\partial}{\partial T_j} |A_{i,k}(\mathbf{T})| \frac{\partial T_k}{\partial x}. \quad (13)$$

When the truncation error equation (4) is scalar, it is a relatively routine exercise to verify that the solution δ to the linearization (12) satisfies the stability estimate $\|\delta(t)\|_{L^1} \leq \|\delta(0)\|_{L^1}$. This follows from standard L^1 theory. Moreover, when the truncation error equation applies to the Euler equations, and when the linearization is carried out around a constant state, δ satisfies the stability estimate $\|\delta(t)\|_{L^2} \leq \text{const} \|\delta(0)\|_{L^2}$. This estimate is easily verified by recalling the fact that the Euler flux Jacobians (hence, the upwind dissipation matrices) can be simultaneously symmetrized. However, this last fact does **not** imply stability of the linearization around a strong shock viscous profile.

Since the grid aligned viscous profile $\mathbf{T}(x)$ has no y component of velocity, the y dissipation matrix $|B(\mathbf{T})|$ is everywhere multiplicity 2 singular. Moreover, the x dissipation matrix $|A(\mathbf{T})|$ is almost singular near the sonic point within the shock layer. (Note that almost singular depends on the amount of smoothing applied to $|f'(\mathbf{U})|$.) In the next several paragraphs we show that these facts combine to lead to a true instability when $\mathbf{T}(x)$ is associated to a strong shock.

We assume 1-periodic boundary conditions in y in which case $\delta(x, y, t)$ takes the form

$$\delta(x, y, t) = \sum_n \alpha_n(x, t) e^{i2\pi n y}.$$

For simplicity, we also assume that $\Delta x = \Delta y$. By rescaling x and t and defining $N_y = 1/(n\Delta y)$, a typical Fourier coefficient $\alpha(x, t)$ is seen to satisfy the one space dimensional equation

$$\frac{\partial \alpha}{\partial t} + \mathcal{L}_{N_y}(\alpha) = 0, \quad (14)$$

where

$$\mathcal{L}_{N_y}(\alpha) = \frac{\partial}{\partial x} \left(f'(\mathbf{T})\alpha - |A(\mathbf{T})| \frac{\partial \alpha}{\partial x} - |A(\mathbf{T})'| \frac{\partial \mathbf{T}}{\partial x} \cdot \alpha \right) + \frac{\pi}{N_y} \left(\mathbf{i}g'(\mathbf{T}) + \frac{\pi}{N_y} |B(\mathbf{T})| \right) \alpha.$$

Note that at the discrete level, N_y represents the number of grid spacings within one period of the associated crossflow mode. Also note that \mathcal{L}_∞ is a singular operator with null vector

$\partial \mathbf{T} / \partial x$. This null vector is associated to the translation invariance of the stationary one-dimensional viscous profile.

We say that the linearization (14) is **unstable** if for some N_y , \mathcal{L}_{N_y} has an eigenvalue λ with negative real part. Owing to the complexity of the **variable coefficient** linearization \mathcal{L}_{N_y} coming from the truncation error equation applied to the Euler equations, the stability of \mathcal{L}_{N_y} is investigated numerically; (14) is discretized in space by central differencing with a variety of grid sizes all taken much less than one. $\mathbf{T}(x)$ is obtained by determining a discrete, one-dimensional, stationary viscous profile to (4) with far-field conditions that correspond to a pressure ratio 10 stationary 1-shock. (This is the data that produced the carbuncle flaws illustrated in the shock tube examples of Section 3.) The tensor $|A(\mathbf{T})|'$ is extremely complicated and is therefore approximated by finite difference ($\Delta T_k = |T_k| 10^{-5}$). The stability of the evolution equation (14) is measured by approximating the value of $\max_{\lambda \in \sigma(\mathcal{L}_{N_y})} |e^{-\lambda}|$ by a method similar to the power method. Specifically, we iterate

$$\alpha_{N_y}^{k+1} = \alpha_{N_y}^k - \Delta \tau \mathcal{L}_{N_y}(\alpha_{N_y}^k),$$

with $\alpha_{N_y}^0 = \partial \mathbf{T} / \partial x$ and with $\Delta \tau \ll 1$ well within the *CFL* limit. After iterating away modes that are least significant, we measure

$$\max_{\lambda \in \sigma(\mathcal{L}_{N_y})} |e^{-\lambda}| \approx \left[\frac{\max_{(x,y)} |(\alpha_{N_y}^K)_1|}{\max_{(x,y)} |(\alpha_{N_y}^{K-1})_1|} \right]^{1/\Delta \tau} \equiv \nu(N_y) \quad \text{with } K \Delta \tau = 10,$$

where $(\alpha)_1$ denotes the density component of α . This measure is reasonable since for large K the major bulk of α is contained in the eigenvector r_λ to \mathcal{L}_{N_y} with eigenvalue λ having the most negative real part. Assuming this eigenvalue is simple,

$$\alpha_{N_y}^K \approx c^K r_\lambda = (I - \Delta \tau \mathcal{L}_{N_y}) c^{K-1} r_\lambda = (1 - \Delta \tau \lambda) c^{K-1} r_\lambda \approx (1 - \Delta \tau \lambda) \alpha_{N_y}^{K-1}.$$

So we are essentially measuring

$$|1 - \Delta \tau \lambda|^{1/\Delta \tau} \approx |e^{-\lambda}|.$$

Figure 7a depicts log scale plots of $\max_{(x,y)} |(\alpha_{N_y}^K)_1| / \max_{(x,y)} |(\alpha_{N_y}^0)_1|$ versus $\tau = k \Delta \tau$ for a variety of crossflow perturbations applied to the one-dimensional, pressure ratio 10,

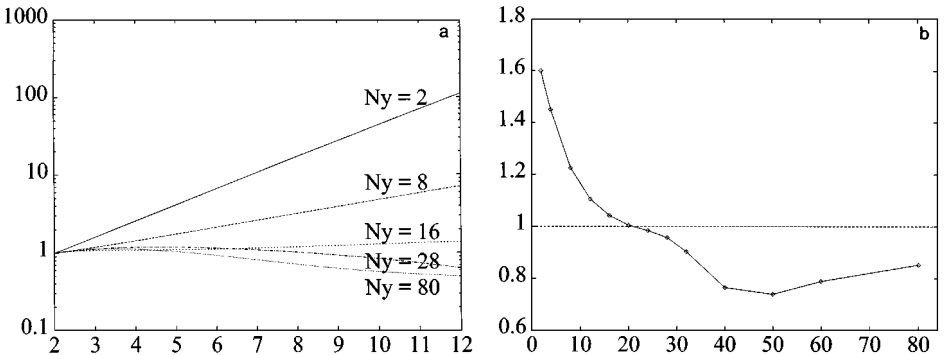


FIG. 7. The (in)stability of the linearized truncation error equation applied to the pressure ratio 10 stationary shock profile: (a) Growth of α_{N_y} vs time τ ; (b) $\nu(N_y)$ vs. N_y .

viscous shock profile. Figure 7b depicts the stability number $\nu(N_y)$ as a function of N_y . Recall that N_y represents the number of Δy grid spacings contained within a crossflow mode. Therefore, $N_y = 2$ is associated to the highest frequency supported by an upwind scheme modeled by the truncation error equation (4). This high frequency mode is clearly unstable. We should note, however, the instability decreases and eventually vanishes when the calculation is performed around weaker shock profiles. Moreover, note that lower frequency crossflow modes ($N_y = 4, 6, \dots$) produce weaker instabilities for the pressure ratio 10 profile, and the instability vanishes for all $N_y > 20$. To confirm that these numerically generated results are real and not due to discretization error or numerical instability, we note that essentially identical results are obtained by reducing the space step size by a factor of 10, as well as reducing the *parabolic CFL* number by a factor of 10.

We admit that the argument presented above does not constitute a mathematical proof that all (or even some) strictly upwind numerical schemes are unstable when applied to strong, stationary, or slowly moving, grid-aligned shocks to the Euler equations in more than one space dimension. Only a generic truncation error equation was considered, and higher order terms that would more accurately describe a particular upwind numerical flux function were neglected altogether. Nevertheless, the linear instability result presented above is in remarkable qualitative agreement with numerical results presented in the literature [15], as well as the unstable shock tube examples presented in the previous section.

5. MULTIDIMENSIONAL DISSIPATION

As mentioned in the last paragraph of the previous section, the studied truncation error equation lacks higher order terms that are necessary to identify a specific one-dimensional upwind numerical flux function. However, this weakness only concerns the flux in the flow (x) direction. Since $\mathbf{T}(x)$ is constant in y for the studied shock tube example, the crossflow (y) flux, based on any one-dimensional strictly upwind flux formulation is indeed accurately modeled in (12). For the Euler equations, the numerical dissipation modeled by $|B(\mathbf{U})|$ is singular when the fluid's y component of velocity is zero, and moreover, this is true in the shock layer where the problem becomes most stiff. We are therefore led to consider a multidimensional modification to the traditional dimension by dimension upwind approach. In this section, we first consider a technique to stabilize the truncation error model problem studied in Section 4. Using this technique as a guide, we develop a very simple multidimensional modification to the Roe's scheme entropy correction techniques (9)–(10) introduced in Section 2, and we show the performance of a modified scheme on the numerical examples used previously to demonstrate instability.

Some observations are in order at this point. First, if the matrix $|A(\mathbf{T})|' \partial_x \mathbf{T}(x)$ in the linearization (12) is neglected, the instability observed in the previous section is eliminated. This is true regardless of the strength of the shock profile that the linearization is performed about. It is also worth noting that if $|A(\mathbf{T})|$ were not smoothed (i.e. cut off from being singular), as was done in the model linearization, the term $\partial_x \mathbf{T}(x)$ would be unbounded at some point within the shock layer. Second, the unstable eigenvectors to the linearized model problem (12) are always highly oscillatory in the crossflow direction. To stabilize the model problem, it seems natural to attempt to damp these characteristic crossflow oscillations. This can be accomplished by the inclusion of additional crossflow

dissipation,

$$|B(\mathbf{T})| = |g'(\mathbf{T})| + d(x, y)I$$

with $d(x, y) > 0$. Note that only the y direction dissipation is modified here, leaving the shock profile $\mathbf{T}(x)$ unaffected. Since one expects the magnitude of $\partial_x \mathbf{T}(x)$ to play a role in the magnitude of the oscillations (instability), it seems natural to take

$$d(x, y) \sim \Delta x \left| \frac{\partial \mathbf{T}}{\partial x} \right|.$$

Terms on the order of $\Delta x \partial_x \mathbf{T}(x)$ are computed by a typical x -directional entropy correction; recall $\eta(\mathbf{U}_L, \mathbf{U}_R)$ in Eq. (10). Therefore, we propose a crossflow dissipation modification to the truncation error model problem given explicitly by

$$|B(\mathbf{T}, \Delta x \partial_x \mathbf{T})| = |g'(\mathbf{T})| + \frac{\Delta x}{2} \max_l \left| \frac{\partial \lambda_l}{\partial x}(\mathbf{T}) \right| I. \quad (15)$$

It is of value to check what effect (15) has on the stability of the linearization to the model truncation error equation studied in the previous section; (15) is indeed a multidimensional dissipation since the y -directional dissipation depends on the solution variation in the x direction. It is worth stressing, however, that this modification leaves the one-dimensional profile $\mathbf{T}(x)$ fixed. Following exactly the same procedure described in Section 4, we calculate the modified model's stability. Figure 8 depicts the growth of most oscillatory crossflow perturbations. Comparing with Fig. 7, we see that previously the mode $N_y = 2$ grew by a factor of 100 in 10 units of time, whereas here it decayed.

The multidimensional modification derived and analyzed above for the model problem is extended to Roe's scheme by the following procedure. Consider a typical cell interface $I_{i+1/2,j}$; see Fig. 9. First compute

$$\eta_{i+1/2,j} = \frac{1}{2} \max_l (|\lambda_l(\mathbf{U}_{i+1,j}, \mathbf{n}_{i+1/2,j}) - \lambda_l(\mathbf{U}_{i,j}, \mathbf{n}_{i+1/2,j})|).$$

Note that $\eta_{i+1/2,j}$ has already been seen in the one-dimensional entropy correction (10). We now propose the following very simple multidimensional modification [10] to the elements

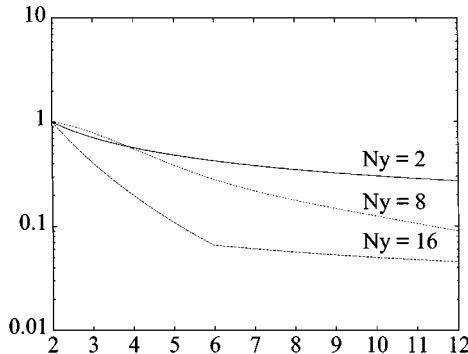


FIG. 8. Growth of α_{N_y} vs time τ for the modified scheme.

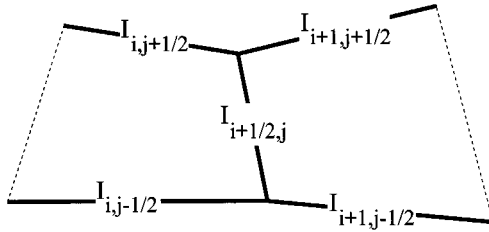


FIG. 9. A two-dimensional cell interface.

$|\tilde{\lambda}_l|$ to the diagonal part of Roe's upwind dissipation matrix in (8.R): For every cell interface, symmetrically calculate

$$\eta_{i+1/2,j}^H = \max(\eta_{i+1/2,j}, \eta_{i,j+1/2}, \eta_{i,j-1/2}, \eta_{i+1,j+1/2}, \eta_{i+1,j-1/2}) \quad (16)$$

and use $\eta_{i+1/2,j}^H$ to determine $|\tilde{\lambda}_l|$ according to one of the entropy corrections suggested in (9). These formulations consist of introducing the largest 1D entropy correction from all neighboring cell interfaces. (We call this the H -correction from its appearance in Fig. 9.) This approach leaves perfectly one-dimensional profiles absolutely unaffected.

We now apply the simple H -corrections (16) to the two Euler equation examples introduced earlier. In both cases, we evaluate the upwind dissipation matrices in (8.R) at the Roe average U_M . The pressure ratio 10 shock tube example from Section 3 is solved this time with the H -correction η^H above, in conjunction with entropy correction (9b). Figure 10a

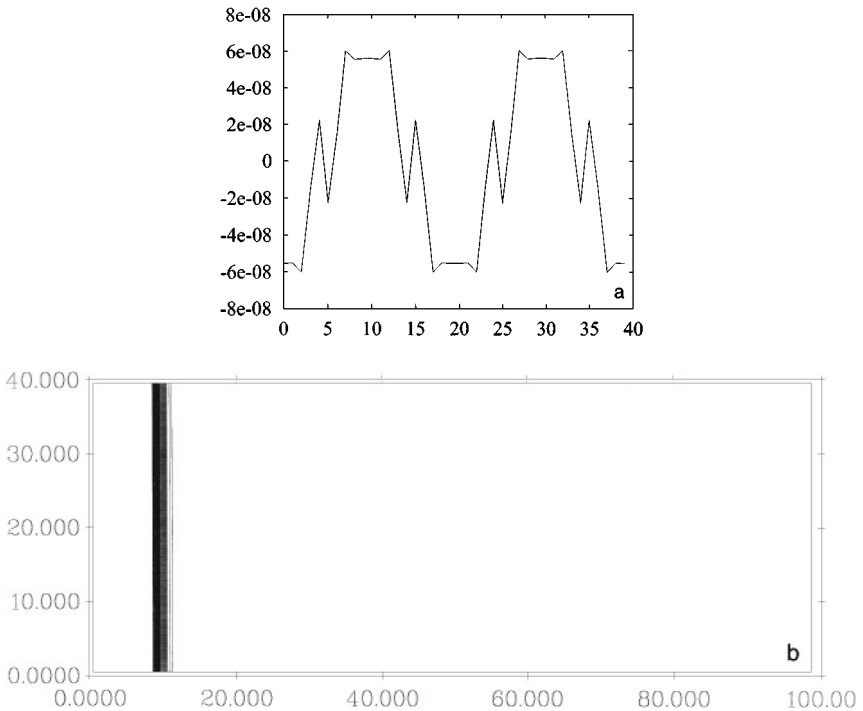


FIG. 10. Results of the pressure ratio 10 shock tube example employing the H -correction: (a) $\rho(11, y, 229) - \rho(11, y, 0)$; (b) Mach number contours at $t = 229.0$.

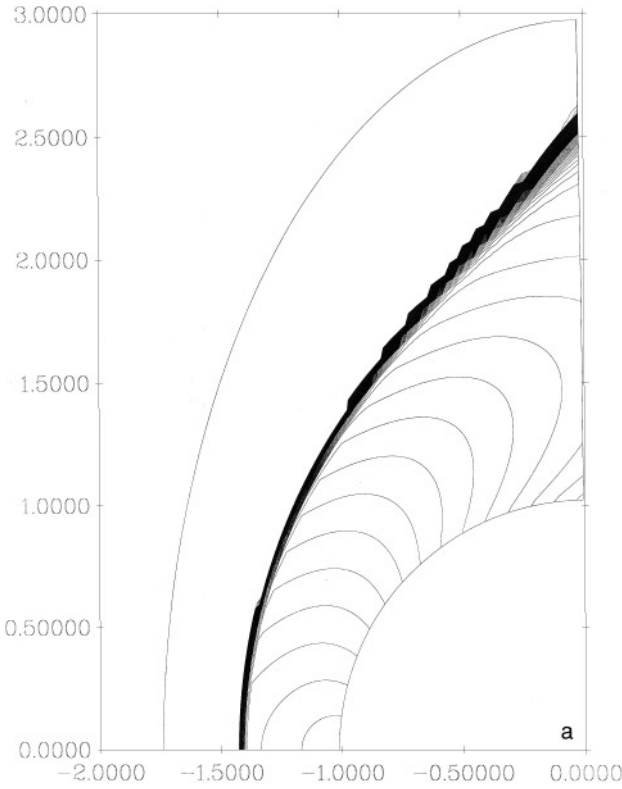


FIG. 11. Contour lines of Mach number for the Mach 15.3 cylinder with Roe's scheme employing the *H*-correction: (a) Only the upper half of the domain is displayed; (b) Close-up of the stagnation point.

depicts the section $\rho(11, y, 229) - \rho(11, y, 0)$. Comparing this to the sections given in Fig. 4, we see the almost complete elimination of the high frequency modes associated to the linear instability. Figure 10b depicts Mach number contours at $t = 229$. The robustness of this new approach was checked and is evidently robust for a variety of shock strengths. Figure 11 depicts the converged solution to the Mach 15.3 flow around a cylinder previously seen in the introduction of this paper, this time, however, using the *H*-correction with (9b). Comparing this to the solution depicted in Fig. 1b, we see that the carbuncle is completely eliminated and the shock is resolved in two points at the point where the flow is grid-aligned.

Additionally, Pandolfi in [12] successfully adapted the *H*-correction to an Osher-like scheme.

6. EXTENSION TO HIGHER ORDER WITH APPLICATION

In order to get accurate results while simulating chemically reacting flows, for example, the numerical method has been upgraded to a second order accurate in space and time version. The second order accuracy in time is performed via a two step Runge–Kutta scheme. High order accuracy in space is achieved by computing \mathbf{U}_R as $\mathbf{U}_{i+1,j}^-$ and \mathbf{U}_L as $\mathbf{U}_{i,j}^+$ given by Turkel and van Leer's $\kappa = 1/3$ reconstruction [19] (done dimension by

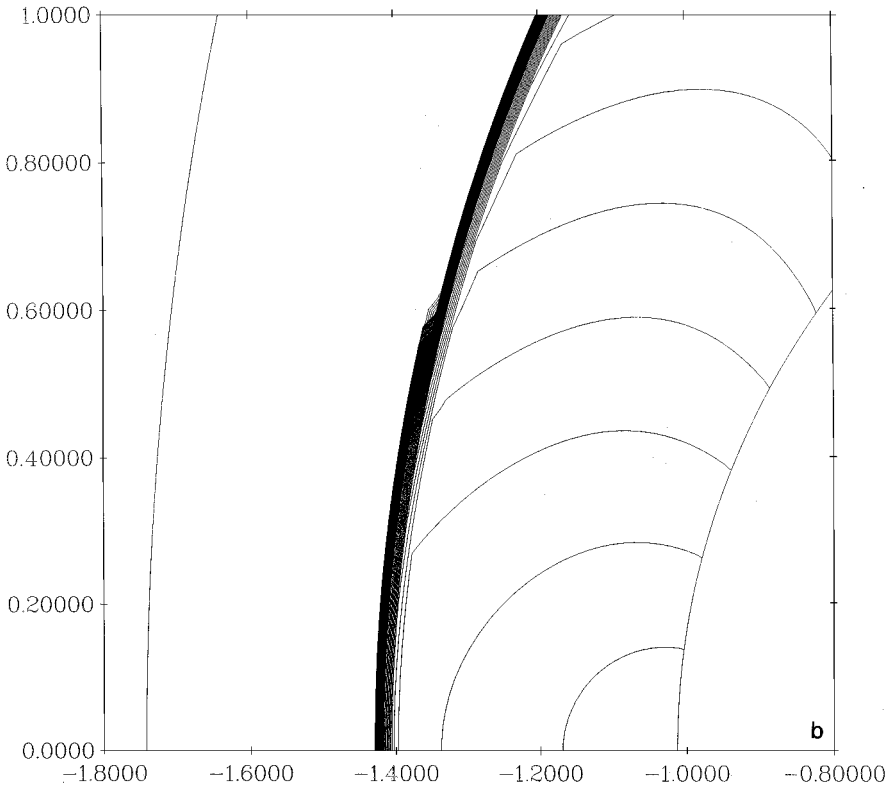


FIG. 11—Continued

dimension),

$$\begin{aligned} \mathbf{U}_{i,j}^- &= \mathbf{U}_{i,j} - \frac{1}{3}\mathbf{S}_{i,j}^- - \frac{1}{6}\mathbf{S}_{i,j}^+ \\ \mathbf{U}_{i,j}^+ &= \mathbf{U}_{i,j} + \frac{1}{3}\mathbf{S}_{i,j}^+ + \frac{1}{6}\mathbf{S}_{i,j}^-, \end{aligned}$$

where

$$\begin{aligned} \mathbf{S}_{i,j}^- &= R \minmod(R^{-1}\Delta\mathbf{U}_{i-1/2,j}, \varpi R^{-1}\Delta\mathbf{U}_{i+1/2,j}) \\ \mathbf{S}_{i,j}^+ &= R \minmod(R^{-1}\Delta\mathbf{U}_{i+1/2,j}, \varpi R^{-1}\Delta\mathbf{U}_{i-1/2,j}) \end{aligned} \quad (17)$$

and where R is the matrix of right eigenvectors to $\partial_{\mathbf{U}}\mathbf{F}$ evaluated at cell centers, and

$$\begin{aligned} \Delta\mathbf{U}_{i-1/2,j} &= \mathbf{U}_{i,j} - \mathbf{U}_{i-1,j} \\ \Delta\mathbf{U}_{i+1/2,j} &= \mathbf{U}_{i+1,j} - \mathbf{U}_{i,j}. \end{aligned}$$

The minmod function reads:

$$\minmod(a, b) = \begin{cases} a & \text{if } |a| < |b|, \ a \cdot b > 0, \\ b & \text{if } |b| < |a|, \ a \cdot b > 0, \\ 0 & \text{if } a \cdot b < 0. \end{cases}$$

In the present work, the computations have been done with $\varpi = 2.0$, which results in a TVD reconstruction for the one-dimensional constant coefficient problem.

The H -correction presented in Section 5.

$$|\tilde{\lambda}_l| = |\lambda_l(\mathbf{U}_M, \mathbf{n})| + \eta_{i+1/2,j}^H$$

is easily extended to this higher order scheme, where the correction $\eta_{i+1/2,j}$ occurring in (16) is computed with the **reconstructed variables** \mathbf{U}_L and \mathbf{U}_R at each cell interface $(i + 1/2, j)$:

$$\eta_{i+1/2,j} = \frac{1}{2} \max_l (|\lambda_l(\mathbf{U}_R, \mathbf{n}_{i+1/2,j}) - \lambda_l(\mathbf{U}_L, \mathbf{n}_{i+1/2,j})|).$$

Note that in order to avoid calculating the true Roe average when evaluating the dissipation matrix $|A(\mathbf{U}_L, \mathbf{U}_R, \mathbf{n})|$ in (8.R), we evaluate $R(\bar{\mathbf{U}}, \mathbf{n})$ and $\lambda(\bar{\mathbf{U}}, \mathbf{n})$ at the simple average $(\bar{\mathbf{U}} = 1/2(\mathbf{U}_L + \mathbf{U}_R))$.

6.1. Chemically Reacting Hypersonic Flows

The higher order scheme above is applied to the computation of compressible nonequilibrium flows. Specifically, we compute a high Mach number flow past a blunt body simulating its reentry into the Earth's atmosphere. Such a simulation requires one to take into account real gas effects and their interaction with the flow dynamics at high velocity and at atmospheric density. It has been shown that by not considering the nonequilibrium effects behind a strong shock wave, very high computed temperature results behind the shock (e.g., 25,000 K temperature behind a Mach 25 shock) and does not correspond to the physical characteristics of the flowfield. One of the most important nonequilibrium effects is the chemical reactions between the different species present in the airflow. Because of the high thermal agitation behind the shock wave, the molecules dissociate. Since the dissociation reactions are endothermic, the temperature behind the shock is lower than that obtained without the chemical reactions. The air behind the shock wave must then be regarded as a mixture composed of the classical 5 species, governed by the usual 17 chemical reactions model, whose chemical rate constants are given by Gardiner's model [3]. Therefore, the partial densities ρ_s appearing in Eq. (5) are $\rho_1 = \rho_{O_2}$, $\rho_2 = \rho_{N_2}$, $\rho_3 = \rho_{NO}$, $\rho_4 = \rho_O$, and $\rho_5 = \rho_N$, and the chemical source vector reads

$$\Omega = (\omega_{O_2}, \omega_{N_2}, \omega_{NO}, \omega_O, \omega_N, \mathbf{0}, 0)^t.$$

Each reaction r can be written as

$$\sum_{s=1}^5 v'_{s,r} A_s \xrightleftharpoons[K_{b,r}(T)]{K_{f,r}(T)} \sum_{s=1}^5 v''_{s,r} A_s, \quad r = 1, \dots, 17,$$

where A_s represents each of the 5 species, $v'_{s,r}$ and $v''_{s,r}$ are the stoichiometric coefficients corresponding to the reaction r and to the species s , and $K_{f,r}(T)$ and $K_{b,r}(T)$ are the forward and backward kinetic rate constants. It follows that the source term of each mass conservation equation, i.e. the mass production rate of each species s , can be written as

$$\omega_s = M_s \sum_{r=1}^{17} (v''_{s,r} - v'_{s,r}) \left[K_{f,r}(T) \prod_{i=1}^5 \left(\frac{\rho_i}{M_i} \right)^{v'_{i,r}} - K_{b,r}(T) \prod_{i=1}^5 \left(\frac{\rho_i}{M_i} \right)^{v''_{i,r}} \right],$$

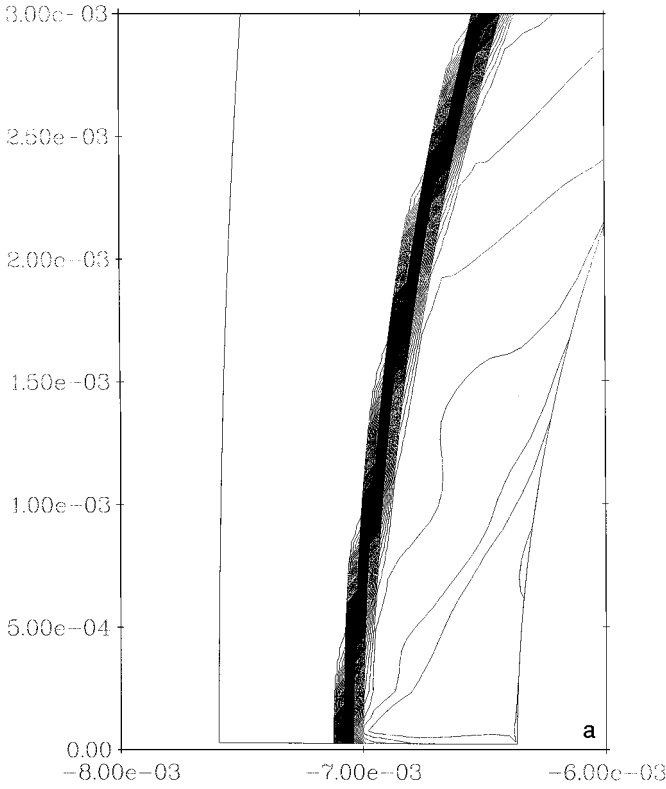


FIG. 12. Mach number isocontours for the 3D axisymmetric Mach 15.3 reacting flow around a sphere—second-order simplified scheme: (a) Typical 1D entropy correction; (b) H -correction.

where M_s is the molar mass of the species s . In Gardiner's model, $K_{f,r}(T)$ is given by

$$K_{f,r}(T) = \alpha_r T^{\beta_r} \exp\left(-\frac{\theta_{D_s}}{T}\right),$$

where α_r and β_r are Gardiner's constants, and θ_{D_s} is the characteristic temperature of dissociation of the molecule s . In order to respect the equilibrium rate $K_{eq,r}(T)$ for the reaction r , the backward kinetic rate constant $K_{b,r}(T)$ is computed as

$$K_{b,r}(T) = \frac{K_{f,r}(T)}{K_{eq}(T)}.$$

One notes that the chemical reaction rate ω_s depends on ρ_s and ϵ via the temperature T that is deduced from the expression of internal energy,

$$\rho e = \rho e - \frac{1}{2} \rho \|\mathbf{V}\|^2 = \sum_{s=1}^5 \rho_s c_{v_s} T + \sum_{s=1}^5 \rho_s h_s^0,$$

where c_{v_s} is the mass heat at constant volume (equal to $\frac{5}{2} R_s$ for diatomic species or $\frac{3}{2} R_s$ for monatomic species), $R_s = (\mathcal{R}/M_s)$ (with \mathcal{R} the perfect gas constant and M_s the molecular mass of the species s); h_s^0 is its heat of formation. The sound speed c is not computed

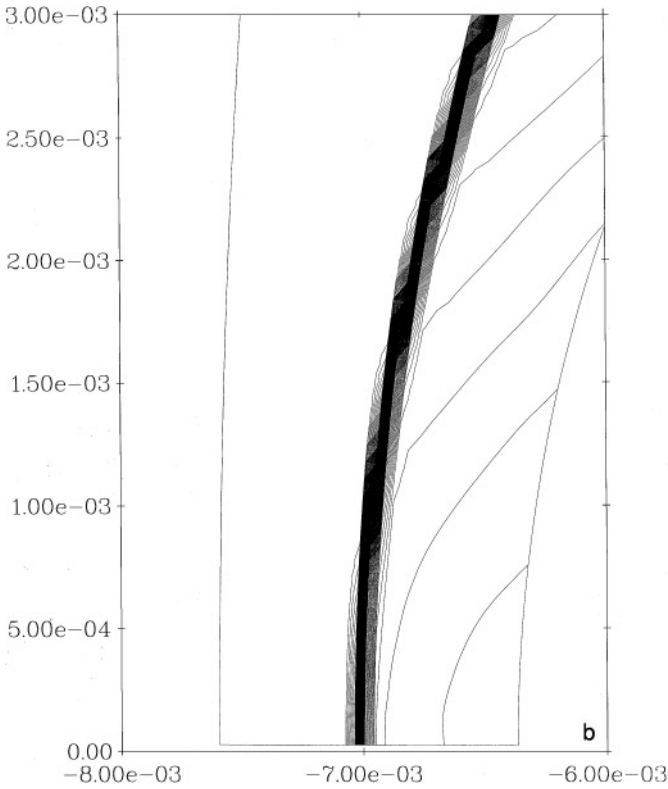


FIG. 12—Continued

through an “equivalent” gamma $\tilde{\gamma}$ formulation, as proposed by Gnoffo in [4], but it is the true sound speed computed from equation (6m), where $P = \sum_s \rho_s R_s T$. The derivatives of P appearing in (6m) include the derivatives of T with respect to ρ_s and to ϵ . These derivatives are obtained by deriving the expression of internal energy with respect to ρ_s and then with respect to ϵ .

6.2. Numerical Results with Chemical Nonequilibrium

To illustrate our work, we present hereafter results of numerical simulation of chemically reactive inviscid hypersonic flow past a 3D axisymmetric sphere whose radius is 6.35 mm. The computational domain is a 96×32 point grid. The upstream conditions are

$$M_\infty = 15.3, \quad P_\infty = 664 \text{ Pa}, \quad T_\infty = 293^\circ \text{K}, \quad X_{O_2\infty} = 21\%, \quad X_{N_2\infty} = 79\%,$$

where X_s is the molar fraction of species s . These conditions correspond to experimental conditions found in Lobb [9]. The computation is carried out by the finite volume method, where the numerical fluxes are computed as outlined above with left and right values reconstructed by the high order method (17). The chemical source terms are treated semi-implicitly with one Newton step applied per time step. Two series of computations have been conducted with: (a) the monodimensional entropy correction (9a); (b) the H -correction variation of (9a). The corresponding results are presented below. The figures

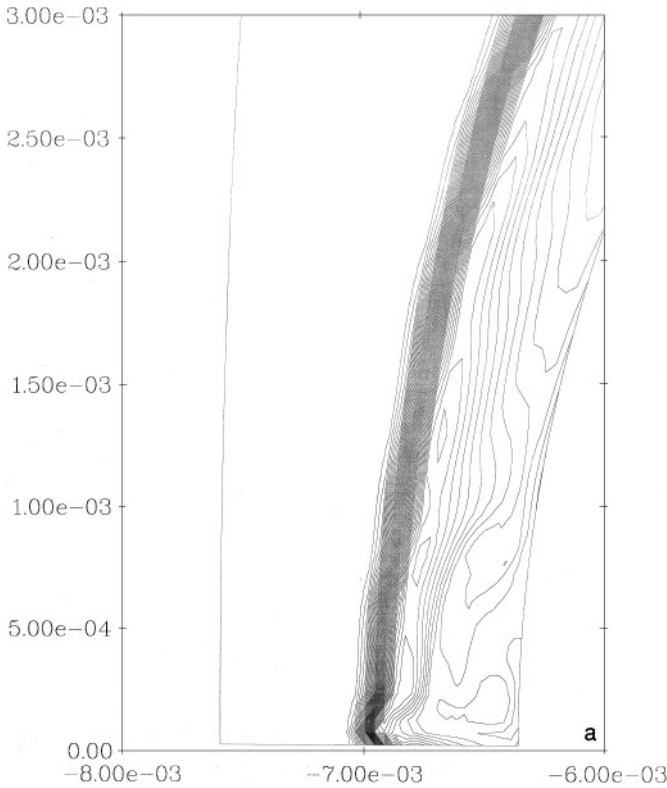


FIG. 13. Molecular nitrogen mass fraction isocontours for the 3D axisymmetric Mach 15.3 reacting flow around a sphere—second-order simplified scheme: (a) Typical 1D entropy correction; (b) H -correction.

only display a fraction of the computational domain focusing on the stagnation point of the flow. First, we show in Figs. 12a and 12b a comparison of Mach number contours obtained, respectively, with the typical monodimensional entropy correction and with the new H -correction method. In Figs. 13a and 13b, we present isocontours of molecular nitrogen mass fraction. Note that in Figs. 12a and 13a, the carbuncle is present but appears much weaker than observed in other examples presented in this paper. This is not a result of the chemistry, but rather typically seen when performing axisymmetric calculations. In Figs. 12b and 13b, there is no trace of the carbuncle coming from the H -correction scheme. These results are comparable to those found in the literature [18].

In the present work, however, we observe that with first-order accurate in space schemes, the atom conservation law is numerically verified, but it is not with high order accurate in space schemes. From this observation, we could say that the nonconservation of atoms comes from the high order reconstruction. Indeed, the slopes $\mathbf{S}_{i,j}^-$ and $\mathbf{S}_{i,j}^+$ may not have the same behavior for each variable ρ_s . Therefore, the minmod function would not apply in the same way to these slopes, and consequently, the ratio of the number of nitrogen atoms to the number of oxygen atoms would no longer be constant. To overcome this problem, we have recomputed two slopes \mathbf{S}^\pm (17) as functions of the other three via the usual expressions of dependance between the five species [1]. With this modification, the atoms are conserved to 10^{-5} , while without modifying the high order reconstruction, the atom conservation was only satisfied to 10%.

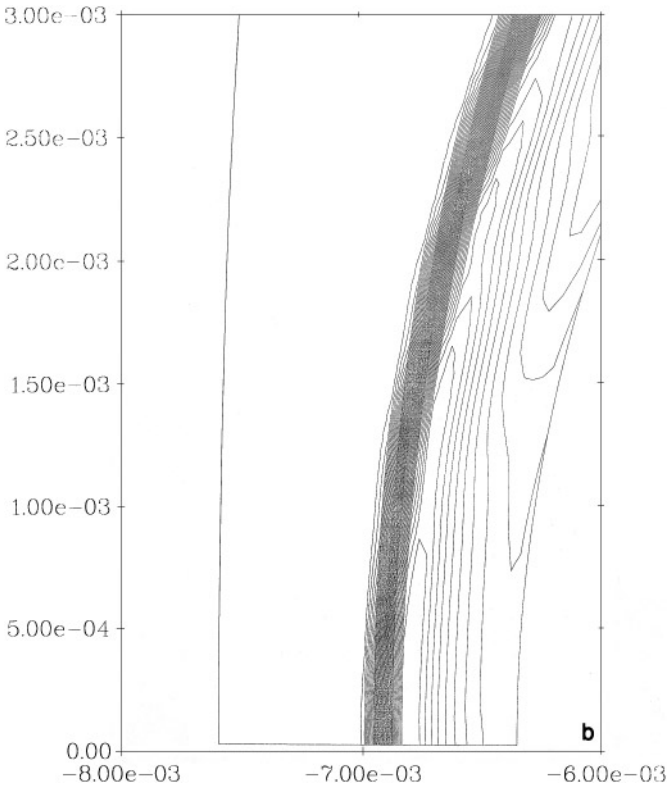


FIG. 13—Continued

ACKNOWLEDGMENTS

The Godunov scheme numerical examples were conducted using Amrita [16] developed by J. Quirk at the California Institute of Technology, Pasadena.

REFERENCES

1. M. C. Druguet, *Contribution à l'étude des écoulements Eulériens hypersoniques en déséquilibre thermo-chimique*, Ph.D. thesis, Université de Provence, Aix-Marseille I, 1992.
2. D. Gaitonde, *High-Speed Viscous Flows Past Blunt Bodies and Compression Corner with Flux-Split Methods*, Wright Laboratory WL-TR-92-3018, 1992.
3. W. C. Gardiner, *Combustion Chemistry* (Springer Verlag, New-York, 1984).
4. P. A. Gnoffo, *Hypersonic Flows over Biconics Using a Variable-Effective-Gamma, Parabolized-Navier-Stokes Code*, AIAA Paper 83-1666, 1983.
5. S. K. Godunov, A finite difference method for the computation of discontinuous solutions to the equations of fluid dynamics, *Mat. Sb.* **47**, 271 (1959).
6. A. Harten, High resolution schemes for hyperbolic conservation laws, *J. Comput. Phys.* **49**, 357 (1983).
7. A. Harten, B. Engquist, S. Osher, and S. R. Chakravarthy, Uniformly high order accurate essentially non-oscillatory schemes III, *J. Comput. Phys.* **71**, 231 (1987).
8. P. D. Lax, Shock waves and entropy, in *Contributions to Nonlinear Functional Analysis*, edited by E. H. Zarantonello (Academic Press, New York, 1971), p. 603.
9. R. K. Lobb, Experimental measurement of shock detachment distance on sphere in air at hypervelocity, *J. Comput. Phys.* (1984). [*Proceedings of the High Temperature Aspect of Hypersonic Flows*, edited by C. W. Nelson, p. 519]

10. E. Morano and R. Sanders, The carbuncle phenomenon: on upwind schemes in multidimensions, *C. R. Acad. Sci. Comput. Fluid Mech.* **325**(II), 339 (1997).
11. S. Osher and F. Solomon, Upwind schemes for hyperbolic systems of conservation laws, *Math. Comp.* **38**, 339 (1982).
12. M. Pandolfi and D. D'Ambrosio, Upwind methods and carbuncle phenomenon, in *Proceedings of the Fourth ECCOMAS Computational Fluid Dynamics Conference, Athens, Greece, September 7-11, 1998* (Wiley, New York, 1998).
13. K. M. Peery and S. T. Imlay, *Blunt-Body Flow Simulations*, AIAA Paper 88-2904, 1988.
14. H. Prue and R. Sanders, On travelling-wave solutions to systems of conservation laws with singular viscosity, *Comm. Partial Differential Equations* **12**, 1285 (1987).
15. J. J. Quirk, A contribution to the great Riemann solver debate, *Int. J. Numer. Methods Fluids* **18**, 555 (1994).
16. J. J. Quirk, Amrita - A computational facility (for CFD modelling), in *VKI 29th Lecture Series, February 23-27, 1998*.
17. P. L. Roe, Approximate Riemann solvers, parameter vectors and difference schemes, *J. Comput. Phys.* **43**, 357 (1981).
18. S. Seror, M. C. Druguet, E. Schall, and D. Zeitoun, A new vibration/exchange reactions coupling model for hypersonic air flows, in *32nd AIAA Thermophysics Conference, Atlanta, June 23-27, 1997*. [AIAA paper 97-2556]
19. E. Turkel and B. van Leer, Flux-vector splitting and Runge-Kutta methods for the Euler equations, in *Ninth Internal. Conf. on Numerical Methods in Fluid Dynamics, Saclay, France, June 1984*.
20. B. van Leer, Flux-vector splitting for the Euler equations, in *Lecture Notes in Physics* (Springer-Verlag, New York/Berlin, 1982), Vol. 170, p. 507.
21. Y. Wada and M-S. Liou, *A Flux Splitting Scheme with High-Resolution and Robustness for Discontinuities*, AIAA Paper 94-0083, 1994.